A simplified analytical model of diamond growth in direct current arcjet reactors

David S. Dandy
Department of Chemical Engineering, Colorado State University, Fort Collins, Colorado 80523

Michael E. Coltrin
*Chemical Processing Sciences Department, Sandia National Laboratories,
Albuquerque, New Mexico 87185*

A simplified model of a direct current arcjet-assisted diamond chemical vapor deposition
reactor is presented. The model is based upon detailed theoretical analysis of the transport
and chemical processes occurring during diamond deposition, and is formulated to
yield closed-form solutions for diamond growth rate, defect density, and heat flux to
the substrate. In a direct current arcjet reactor there is a natural division of the physical
system into four characteristic domains: plasma torch, free stream, boundary layer,
and surface, leading to the development of simplified thermodynamic, transport, and
chemical kinetic models for each of the four regions. The models for these four regions
are linked to form a single unified model. For a relatively wide range of reactor operating
conditions, this simplified model yields results that are in good quantitative agreement
with stagnation flow models containing detailed multicomponent transport and chemical
kinetics. However, in contrast to the detailed reactor models, the model presented here
executes in near real-time on a computer of modest size, and can therefore be readily
incorporated into process control models or global dynamic loop simulations.

I. INTRODUCTION

Of the high growth rate deposition technologies for
the synthesis of diamond via low-pressure (<1 atm)
chemical vapor deposition, direct current (dc) arcjet
reactor systems have been demonstrated to be extremely
robust at producing high quality, relatively large area
films.[1-3] A number of theoretical models have been
developed for idealized straining flow,[4] stagnation
flow,[5] and one-dimensional boundary layers[6] in dc
arcjet reactors that capture the multicomponent transport
and detailed homogeneous and heterogeneous chemical
kinetics occurring in these systems. These models in
general agree well with one another and with available
experimental data on growth rate and film quality; the
models have been employed to examine the gas-phase
chemistry leading to several potential growth species,[5,6]
and to identify operating conditions that yield maximum
diamond growth rate.[5]

Through continued use of these models for the
simulation of actual dc arcjet reactors and detailed
analysis of transport and chemical kinetic processes
taking place during diamond growth in these highly
convective environments,[7-9] it has been demonstrated
that the dominant physics of the gas-phase and gas-
surface processes can be captured by making specific
and restrictive assumptions regarding the behavior of the
system. Although the detailed reactor models employed
to simulate dc arcjet systems provide predictive physical
insight, it is also desirable to develop simplified models

of the dc arcjet system, given the observation that
simplified models do indeed capture the essential physics
of the processes. First, the detailed reactor models are
generally very complex and difficult to set up; the ability
to obtain a converged numerical solution depends not
only on the operating conditions specified but also upon
the initial "guess" for the true solution presented to
the iterative solver. Second, these models can require
anywhere from several to tens of minutes to successfully
execute, and therefore are difficult to incorporate directly
into intelligent process control design algorithms.

The motivation of the present work is development
of a simplified physical model of the processes occur-
ring in a dc arcjet reactor, a model free of numerical
instabilities or convergence problems, and one that runs
in near real-time. The present model executes in less
than a millisecond on a fast workstation, approximately
10^5 times faster than the detailed numerical model.[5]
Given a specific set of reactor operating conditions, the
model predicts heat flux to the substrate, diamond growth
rate, and point defect fraction in the diamond phase.
The model in this work builds upon earlier analysis[7,8]
and is validated against detailed transport and kinetic
calculations.[5,6]

II. MODEL FORMULATION AND USE

A schematic diagram of a generic dc arcjet reactor is
illustrated in Fig. 1. In the system under study, pure H_2 is
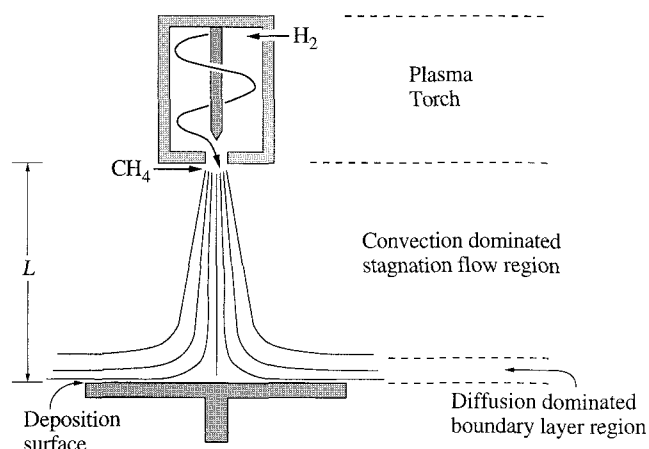fed into the plasma torch, where it undergoes dissociation

FIG. 1. Schematic diagram of the plasma torch/substrate configuration. The system is divided into four submodels: plasma torch, free stream, boundary layer, and surface.

due to the high temperature and through interaction with the plasma. Although the analysis presented below is based upon the presumption that the torch feed gas is pure H_2, it would be straightforward to extend this theory to systems containing unreactive gases such as Ar.[9] The high-velocity jet issuing from the plasma torch is mixed with a hydrocarbon, CH_4 in this study, and sometimes a stream of H_2, and directed toward a temperature-controlled deposition surface, which is located a distance L away from the plasma torch exit orifice. Injecting H_2 downstream of the exit orifice provides independent control of gas temperature and composition, and can be used as the mechanism for delivery of the hydrocarbon into the system.[1] The average velocity of the gas exiting the torch is given by $U_\infty = \dot{m}_{H_2}/(\rho A_s)$, where $\dot{m}_{H_2}$ is the mass flow rate of H_2 through the torch, ρ is the gas density, and A_s is the cross-sectional area of the exit orifice. Due to the relatively low pressures considered in this study ($P \leq 60$ Torr), the H and H_2 concentrations remain nearly constant in the free stream during transit to the surface. The single-carbon species rapidly equilibrate themselves subject to the H and H_2 concentrations, and undergo partial conversion to the thermodynamically favored species, C_2H_2. Only when the gas gets very close to the substrate, usually within 0.5 cm, does the H atom concentration change, dropping rapidly through a boundary layer due to heterogeneous destruction at the substrate. At the substrate deposition reactions of the hydrocarbon species occur, leading to the growth of diamond, as well as the formation of possible lattice imperfections.

The natural division of the physical system into four characteristic domains: plasma torch, free stream, boundary layer, and surface, led to the development of simplified thermodynamic, transport, and chemical kinetic models for each of the four regions. In Secs. II. A–II. D

these models are presented, and representative calculations are carried out using them.

A. Plasma torch

The complexity of the physical processes occurring inside a dc plasma torch preclude the formulation of a comprehensive, tractable model describing the details of the hydrodynamics, chemical kinetics, and charged species interactions. However, it is possible to relate a plasma torch model to diamond deposition, without having to know the details of the torch processes; it is sufficient to specify the conditions (temperature and composition) of the gas mixture leaving the torch given knowledge of the input parameters to the torch (H_2 feed rate and power). Because electron densities are typically low in dc arcjet systems, it is reasonable to assume that the only species leaving the plasma torch are H and H_2. And by making one further assumption it is possible to construct a simple thermodynamic model representing the plasma torch.

The thermodynamic model, represented schematically in Fig. 2, is based upon the treatment of the plasma torch as a well-mixed, steady, open-flow system. The actual energy input to the system through the arc discharge is modeled as a heat flux into the system. This assumption is not rigorously correct because the actual discharge is a volumetric energy source that will be represented as a heat flux into the plasma torch; that is, the heat transfer into the system actually occurs within the plasma torch itself (from the arc discharge), but this heat input will be modeled as if it were transported across the boundaries of the torch.
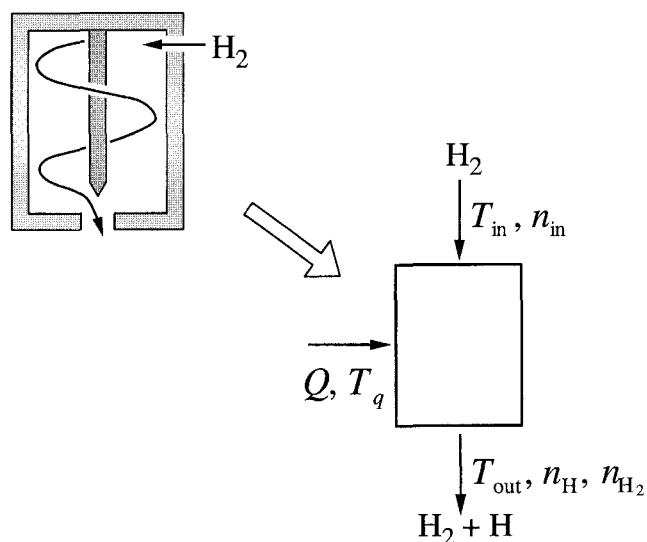

FIG. 2. Schematic diagram illustrating the thermodynamic model utilized to describe the gas heatup and H_2 dissociation occurring in the plasma torch.

The plasma torch model is constructed such that the outlet temperature of the gas mixture, T_{out}, is specified, as is the power input to the plasma torch, Q. The thermodynamic model will then predict the necessary molar flow rate of H_2 input to the plasma torch, $\dot{n}_{in}$, and the degree of dissociation of H_2 occurring in the torch (represented by the molar flow rates of H and H_2 out of the torch, $\dot{n}_H$ and $\dot{n}_{H_2}$). Because there are two unknown quantities in this system, it is convenient to impose as mathematical constraints the first and second laws of thermodynamics. For this steady, open system, it is reasonable to neglect kinetic and potential energy changes of the gas flowing through the torch because they account for less than 1% of the total energy, and the first law of thermodynamics reduces to

$$\dot{Q} = H_{out}\dot{n}_{out} - H_{in}\dot{n}_{in},\qquad(1)$$

where H_{out} and H_{in} are the molar enthalpies of the gas mixture leaving the torch and the H_2 flowing into the torch, respectively, and $\dot{n}_{out} = \dot{n}_H + \dot{n}_{H_2}$. Assuming that the gas mixture leaving the torch is ideal, the mixture molar enthalpy can be computed as the sum of the pure-species molar enthalpies:

$$H_{out} = \sum_i x_i H_i = x_H H_{H_{out}} + x_{H_2} H_{H_{2,out}},\qquad(2)$$

where x_H is the mole fraction of H in the binary mixture exiting the plasma torch. A mass balance on the plasma torch yields a link between the outlet total molar flow rate and the inlet molar flow rate of H_2,

$$\dot{n}_{out} = \frac{2}{2 - x_H}\dot{n}_{in}.\qquad(3)$$

Substituting (3) and (2) into (1), an expression is obtained containing the two unknown quantities, x_H and $\dot{n}_{in}$:

$$\dot{Q} = (x_H H_{H_{out}} + x_{H_2} H_{H_{2,out}})\frac{2}{2 - X_H}\dot{n}_{in} - H_{in}\dot{n}_{in}.\qquad(4)$$

Application of the second law of thermodynamics to this steady, open flow system yields

$$\frac{\dot{Q}}{T_q} = S_{out}\dot{n}_{out} - S_{in}\dot{n}_{in} + \dot{S}_{gen},\qquad(5)$$

where $\dot{S}_{gen}$ is the total molar rate of entropy generation within the plasma torch due to irreversibility, and S_{out} is the molar entropy of the mixture leaving the torch. For an ideal gas mixture,

$$\begin{aligned}
S_{out} &= \sum_i x_i S_i - R\sum_i x_i \ln x_i - R\sum_i x_i \ln(P/P_{atm})\\
&= x_H S_{H_{out}} + x_{H_2} S_{H_{2,out}} - R[x_H \ln(P_H/P_{atm})\\
&\quad + x_{H_2} \ln(P_{H_2}/P_{atm})]
\end{aligned}\qquad(6)$$

where P is the total pressure, P_i is the partial pressure of species i, and P_{atm} is atmospheric pressure. The quantity T_q is the temperature at which heat is transferred into the system, and is taken to be the average of the arc temperature and the mean gas temperature at the torch exit. The entropy generation rate is evaluated as

$$\dot{S}_{gen} = \int_V \dot{\sigma}_s \, dV,\qquad(7)$$

with $\dot{\sigma}_s$ defined to be the local volumetric entropy generation rate. For a nonisothermal flow system where Fourier's law of heat conduction and Newton's law of viscosity are both valid, the volumetric entropy generation rate is[10]

$$\dot{\sigma}_s = \frac{\lambda}{T^2}(\nabla T)^2 + \frac{\mu}{T}\phi^2,\qquad(8)$$

where λ and μ are the mixture thermal conductivity and dynamic viscosity, respectively, and

$$\phi^2 = \sum_i \sum_j \left[\frac{\partial v_i}{\partial x_j} + \frac{\partial v_j}{\partial x_i} - \frac{2}{3}\delta_{ij}(\nabla \cdot \mathbf{v})\right]^2.\qquad(9)$$

In (9), v_i are the components of the velocity vector $\mathbf{v}$, and δ_{ij} is the index representation of the identity tensor, such that $\delta_{ij} = 1$ when $i = j$ and 0 otherwise.

Although the environment inside the plasma torch is highly convective and extremely energetic, a very small error is introduced if $\dot{S}_{gen}$ is neglected in Eq. (5). Order of magnitude analysis of Eqs. (8) and (9) at torch operating temperatures of 3000, 5000, and 8000 K, and $\dot{n}_{in} = 0.10$ to 0.25 mole/s indicate that (i) the contribution to $\dot{S}_{gen}$ from the first term in (8) is less than 2% of the magnitude of the expression $(S_{out}\dot{n}_{out} - S_{in}\dot{n}_{in})$ in Eq. (5) for temperature changes as high as 8000 K over distances as small as 0.1 cm, that is, for temperature gradients as high as 8×10^4 K/cm; and (ii) the contribution to $\dot{S}_{gen}$ from the second term in (8) is less than 0.1% of the magnitude of the expression $(S_{out}\dot{n}_{out} - S_{in}\dot{n}_{in})$ in Eq. (5) for axial, radial, and azimuthal velocity changes as high as 10^5 cm/s over distances as small as 0.1 cm, that is, for velocity gradients as high as 10^6 s^{-1}. Based upon this analysis, $\dot{S}_{gen}$ is dropped from (5) in subsequent use of the model.

Equations (4) and (5) comprise a set of two independent equations that can be used to solve for two unknowns. Because of the transcendental nature of Eq. (6), the system must be solved iteratively. It was found in tests of this model that a Newton's method formulation converged within four iterations; and convergence behavior was not strongly dependent upon the initial guesses for the two unknowns.

Characteristic examples of predictions of the arc-jet model are given here. Figure 3 shows that the
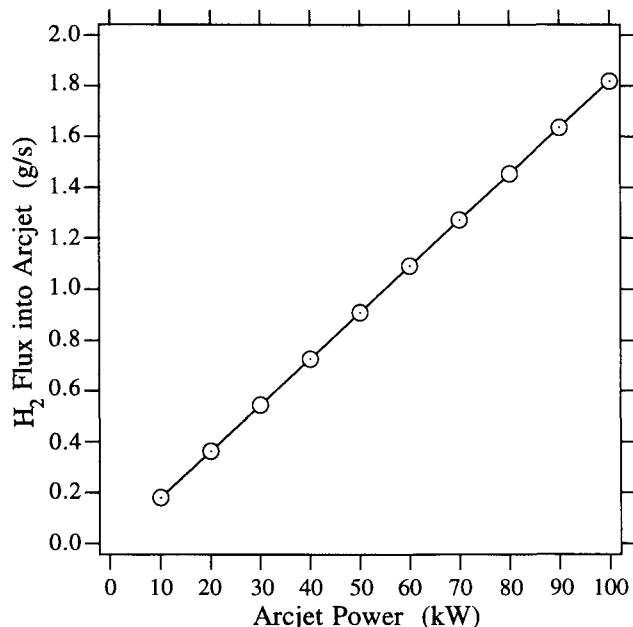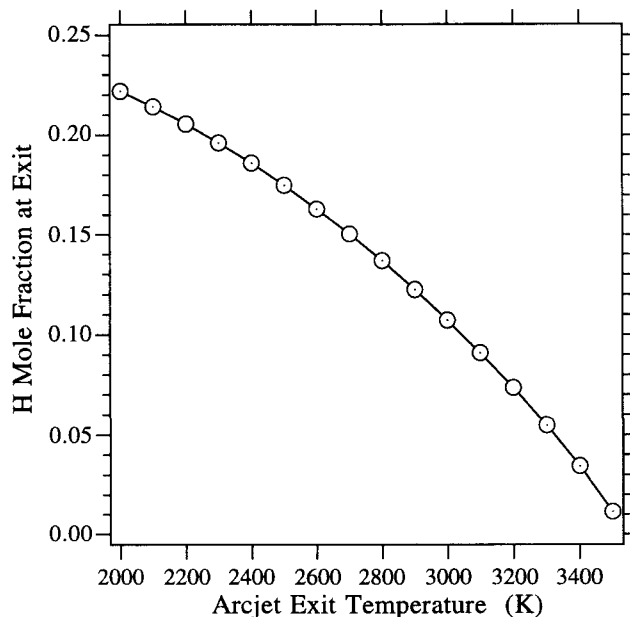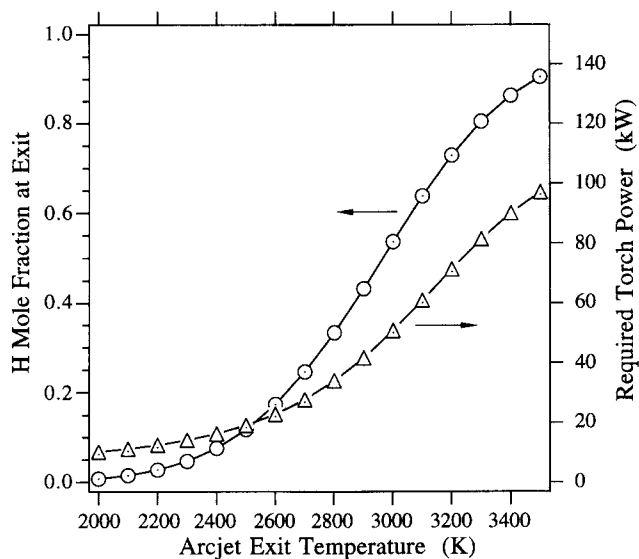
FIG. 3. Torch model prediction of the amount of inlet hydrogen required to produce a 2500 K, 30 Torr $H-H_2$ mixture, as a function of arcjet power.

(a)

(b)

FIG. 4. Torch model predictions of (a) the fraction of the gas jet leaving a 25 kW plasma torch as atomic hydrogen, the remainder being H_2, as a function of desired gas temperature; (b) the fraction of gas leaving a plasma torch as atomic hydrogen and the torch power required to achieve this degree of dissociation, for fixed inlet H_2 flow rate, as a function of desired gas temperature.

amount of H_2 flux into the arcjet increases linearly with torch power, for a specified (fixed) temperature of the gas exiting the arcjet, and fixed total pressure. The fractional dissociation of H_2 remains virtually constant over the range of conditions in Fig. 3. The hydrogen dissociation fraction is a strong function of the exit-gas temperature, as illustrated in Fig. 4(a). For fixed arcjet power, the fractional dissociation of H_2 drops as the gas exit temperature increases; this is because more energy goes into heating the gas from its inlet temperature, at the expense of the energy available to dissociate the molecular hydrogen. In Fig. 4(a) the arcjet power and exit temperature, T_{out}, are specified, and the flow rate of H_2 into the torch and mole fraction of H leaving the torch are computed such that Eqs. (4) and (5) are satisfied. For the conditions shown in Fig. 4(a), energy conservation dictates that the amount of H leaving the torch may not coincide with the concentration it would attain if it were at chemical equilibrium at the torch exit temperature and pressure.

The torch model may be reformulated such that it is assumed that H and H_2 reach chemical equilibrium at the torch exit conditions for fixed inlet H_2 flow and torch power is then computed so that the first law is satisfied. As an example of this reformulation, a reactor pressure of 30 Torr is assumed, and x_H and $\dot{Q}$ are computed. As shown in Fig. 4(b), both of these quantities increase dramatically as T_{out} increases; by assuming that an increased exit temperature is achieved *and* that the mixture reaches chemical equilibrium, a

greater demand for energy (torch power) is required. The reformulated arc model is not realistic in the sense that it doesn't properly account for where the energy goes in the system—the model forces exactly the right amount of energy to go into dissociation such that chemical equilibrium is achieved at the exit conditions. The model represented by Eqs. (4) and (5) allows energy to go

into heating and dissociation in the right combination such that the first and second laws are obeyed. For $T_{out} < 2600$ K the arc model results of Fig. 4(a) yield a superequilibrium of H (greater than chemical equilibrium at T_{out} and P), while for $T_{out} > 2600$ the model predicts subequilibrium concentrations of H in the free stream. This particular transition at 2600 K between sub- and superequilibrium H is a consequence of the torch power used in that calculation, 25 kW. This temperature would change for a different torch power. For a fixed torch power this transition must occur because as the desired exit temperature is increased more of the input energy goes into gas heating, and consequently less of this energy can go into H_2 dissociation.
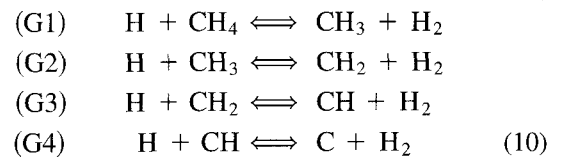
B. Free stream region

The free stream region, the portion of the system between the plasma torch exit and the top of the boundary layer, is characterized by a high-velocity, moderately high Reynolds number ($100 \leqslant \text{Re} \leqslant 300$) flow. Although the jet issuing from the plasma torch has a high velocity, typically between 5×10^4 and 3×10^5 cm/s, the flow is laminar because of the moderate reactor pressures and high gas temperatures utilized in these systems. In this work, reactor pressures ranging from 5 to 60 Torr are considered; in this range the free stream flow is subsonic, with Mach numbers significantly below unity. At pressures lower than approximately 5 Torr, however, a significant portion of the flow region may be trans- or supersonic, with multiple transverse and oblique shocks present. While the model presented in this section for the free stream region does not capture the details of the hydrodynamics, it does rely on the assumption that the flow is incompressible, such that the speed of sound is infinite and the pressure is therefore uniform. Thus, there is no provision in the analysis for pressure, density, or temperature discontinuities.

The free stream model is based upon the knowledge that, as a consequence of the known hydrocarbon combustion kinetics in the diamond system, the gas-phase hydrocarbon species exist in a pseudo-chemical equilibrium state in the region between the plasma torch and the boundary layer edge. (The hydrocarbons are not in chemical equilibrium within the thin boundary layer; a model for this region is discussed in the next section). It is assumed here that once the high velocity H/H_2 mixture exits the plasma torch it is rapidly mixed with an injected CH_4 feed. Although a "superequilibrium" concentration of H is formed in the plasma torch, the relatively low reactor pressure precludes appreciable recombination of H during the short time the gas is in transit to the substrate. The residence time of the gas species in the region between plasma torch and substrate depends on

the separation distance, but, for example, for a 10 cm gap these times vary between 40 and 200 μs. Once CH_4 is mixed with the torch gas, pyrolysis reactions drive the CH_x species ($x = 0$–4) to very quickly equilibrate around the concentrations and H and H_2. Homogeneous kinetic calculations and stagnation flow calculations[4–6] indicate that the equilibration of the C1 species takes place within 15 to 35 μs, and that, at the lowest pressures considered (5–10 Torr) the C1 distribution essentially remains frozen at these values until the gas mixture reaches the boundary layer. At higher pressures (45–60 Torr), however, once the C1 species equilibrate around [H] and [H_2] there is significant conversion to C_2H_2 and, to a lesser extent, C_2H_4, in the free stream region. Therefore, the free stream model is composed of two parts: a partial equilibrium model that predicts the distribution of C1 species for fixed concentrations of H and H_2; and an adjustment of the equilibrium values of the C1 manifold to account for their conversion to C2 species.

To determine the equilibrium concentrations of the C1 species in the free stream, a partial equilibrium model is written involving the four hydrogen abstraction reactions:

(G1) $\quad$ H + CH_4 $\Longleftrightarrow$ CH_3 + H_2

(G2) $\quad$ H + CH_3 $\Longleftrightarrow$ CH_2 + H_2

(G3) $\quad$ H + CH_2 $\Longleftrightarrow$ CH + H_2

(G4) $\quad$ H + CH $\Longleftrightarrow$ C + H_2 $\qquad$ (10)

Given the moles of the three species present at the exit of the arcjet, $\dot{n}_0 = \dot{n}_H + \dot{n}_{H_2} + \dot{n}_{CH_4}$, it is possible to write expressions relating the mole fractions of all species in (10) to the extent of reaction of each reaction, ϵ_i:

$$x_{CH_4} = \frac{\dot{n}_{CH_4} - \epsilon_1}{\dot{n}_0} \quad x_{CH_3} = \frac{\epsilon_1 - \epsilon_2}{\dot{n}_0} \quad x_{CH_2} = \frac{\epsilon_2 - \epsilon_3}{\dot{n}_0}$$

$$x_{CH} = \frac{\epsilon_3 - \epsilon_4}{\dot{n}_0} \quad x_C = \frac{\epsilon_4}{\dot{n}_0} \quad x_H = \frac{\dot{n}_H}{\dot{n}_0} \quad x_{H_2} = \frac{\dot{n}_{H_2}}{\dot{n}_0}$$

$$(11)$$

In formulating (11) it is assumed that [H] and [H_2] remain frozen such that the H recombination reaction, H + H + M $\Longleftrightarrow$ H_2 + M, can be neglected. In this analysis it is further assumed that the injected hydrocarbon concentrations are sufficiently low that they not significantly decrease the concentration of H through participation in the pyrolysis reactions in (10). For the cases considered here the hydrocarbon species make up, at most, 1% of the mixture, and the reactions in (10) will have only a perturbative effect on [H] and [H_2]. At equilibrium, a relationship between the mole fractions of species (and therefore the extents of reaction) can be

written,

$$K_1 = \frac{\dot{n}_{H_2}}{\dot{n}_H} \frac{\epsilon_1 - \epsilon_2}{\dot{n}_{CH_4} - \epsilon_1} \qquad K_2 = \frac{\dot{n}_{H_2}}{\dot{n}_H} \frac{\epsilon_2 - \epsilon_3}{\epsilon_1 - \epsilon_2}$$

$$K_1 = \frac{\dot{n}_{H_2}}{\dot{n}_H} \frac{\epsilon_3 - \epsilon_4}{\epsilon_2 - \epsilon_3} \qquad K_4 = \frac{\dot{n}_{H_2}}{\dot{n}_H} \frac{\epsilon_4}{\epsilon_3 - \epsilon_4}$$

(12)

where K_i are the equilibrium constants for the four reactions, $-RT \ln K_i = \Delta G_i^\circ$, and ΔG_i° is the standard Gibbs energy change of reaction i at temperature T and 1 atm pressure. Equation (12) comprises a linear system for the four unknowns, the extents of reaction. This system can be solved analytically to yield explicit relationships for the ϵ_i, and using (11), the equilibrium mole fractions of the C1 species, plus H and H_2. Detailed kinetic calculations were carried out using the full gas-phase pyrolysis mechanism,[11] to examine whether or not all of the reactions listed in (10) are sufficiently fast in both the forward and reverse directions to achieve equilibrium. It was found that, for the values of T_{out} and P considered here, the forward and reverse rates were fast, and the rate of progress of each reaction (the difference between the forward and reverse rate) was orders of magnitude smaller than either the forward or reverse rate. Thus it is reasonable to assume that all four of the reactions reach constrained equilibrium.

Rigorously accounting for the conversion of the C1 species to the C2 species would require integrating the mass-action expressions arising from the full set of gas-phase pyrolysis reactions over the time the species spend in the free stream region. However, since the intent of this work is to develop simple models for the dc arcjet system, it is advantageous to use experience gained in running detailed stagnation flow simulations to guide the formulation of a simple C1-to-C2 conversion model. To accomplish this objective, the SPIN computer program[12] was employed to examine arcjet deposition over a range of pressures ($5 \leq P \leq 60$ Torr), torch gas exit temperatures ($2000 \leq T_{out} \leq 3500$ K), free stream atomic hydrogen concentrations ($0.05 \leq x_H \leq 0.4$), and inlet CH_4 mole fractions ($0.001 \leq x_{CH_4}^0 \leq 0.03$). The conclusions from these calculations were that (i) C_2H_2 is by far the dominant C2 species, and only small amounts of the higher hydrocarbons are formed for these conditions; (ii) the conversion of C1 species to C_2H_2 is maximized as pressure and H fraction are increased; (iii) conversion of C1 species to C_2H_2 is negligible at low pressure and/or low x_H; (iv) C_2H_2 is thermodynamically favored over other C2 an C1 species over the entire temperature range considered; and (v) the impact of $x_{CH_4}^0$ on C_2H_2 formation is dependent on x_H. For all of the conditions considered in the SPIN calculations, a single reaction was primarily responsible for the formation of C_2H_2: $C + CH_3 \rightarrow C_2H_2 + H$. The

same result was obtained using two different pyrolysis mechanisms in side-by-side comparisons.[11,13] There are other $CH_x + CH_y$ reactions occurring in the free stream, but their predicted rates of progress are all less than 20% that of the methyl plus carbon atom reaction. There are two basic reasons for this finding. First and foremost, for all conditions considered CH_3 and C are predicted to be the dominant single-carbon radicals in the free stream. When the amount of atomic hydrogen in the free stream is less than approximately 20% of the mixture, CH_3 is the prevalent hydrocarbon species, and for atomic hydrogen fractions greater than this, C is prevalent. Second, C_2H_2 is the thermodynamically favored C2 species in the free stream region, and the reaction between carbon atom and methyl radical produces this species directly. Reactions producing species other than acetylene must be followed by an addition reaction (in the case of CH and C) or abstraction reactions. While these abstraction reactions are faster than the $CH_x + CH_y$ coupling reactions, they nevertheless increase the time required to form C_2H_2.

Because it was found from carrying out detailed kinetics calculations that the fractional contribution of this reaction to C1 losses was nearly constant for all conditions considered, a "C1 adjustment model" is imposed on the system. This model capitalizes on the kinetic behavior of the C1 species in the free stream: specifically, it is assumed that the C1 species are rapidly coupled by the hydrogen exchange reactions in (10), and that the hydrogen exchange reactions are fast compared to the bimolecular reactions between the carbon species. Finally, it is assumed that the CH_x ($x = 0, \ldots 4$) relative concentration distribution is independent of the total amount of C1 species present. If C_2H_2 is formed primarily through the reaction $C + CH_3 \rightarrow C_2H_2 + H$, then at any time the instantaneous rate of change of [C] due to this reaction is given by $d[C]/dt = -k[C][CH_3]$, where the rate constant in this expression is taken from the two pyrolysis mechanisms to have zero activation energy and a pre-exponential $A = 5 \times 10^{13}$ cm^3 mole^{-1} s^{-1}. Because the distribution of the C1 species is assumed independent of the total C1 concentration, [CH_3] and [C] are related to one other through a constant, that is, [CH_3] = β[C], where β depends on temperature and the ratio [H_2]/[H]. Thus, the rate of change of [C] can be written as $d[C]/dt = -\beta k[C]^2$. If this rate equation is integrated from an initial equilibrium concentration [C]$_0$ at time $t = 0$, the following expression for [C] at arbitrary time t is obtained:

$$[C] = \frac{[C]_0}{1 + \beta k t [C]_0}.$$

(13)

The length of time that the bimolecular reaction proceeds is $\tau_v = L/U_\infty$, which is the approximate residence time of the gas mixture in the free stream, and is therefore an

estimate of the time required for the gas to travel from the plasma torch exit to the outer edge of the boundary layer. Here, L is the torch-substrate separation and U_∞ is the mass-average velocity of the gas issuing from the plasma torch. The amount of C_2H_2 formed over the time τ_v is then $[C_2H_2] = [C]_0 - [C]$. Because the C1 reactants in the bimolecular reaction are coupled through the hydrogen exchange reactions, an estimate for $[C]_0$ is obtained by assuming $[C]_0 + [CH_3]_0 = [CH_4]^0$, where $[CH_4]^0$ is the concentration of injected methane. Once $[C_2H_2]$ is known at time τ_v, an atom balance on carbon results in a constraint on the total concentration of C1 species,

$$\sum_{x=0}^{4}[CH_x] = [CH_4]^0 - 2[C_2H_2],$$

and the equilibrium distribution of the C1 species may be recomputed according to Eq. (12).

C. Boundary-layer region

The two-part free stream model described in II. B, equilibrium distribution of the C1 species followed by an adjustment to account for conversion to C_2H_2, results in a prediction of the CH_x, C_2H_2, H, and H_2 mole fractions at the outer edge of the boundary layer, that is, at a position close to the substrate where a transition from convection-dominated to diffusion-dominated transport occurs. In the dc arcjet system there are actually three distinct boundary layers: momentum, thermal, and concentration. The momentum boundary layer arises because of the sharp drop in axial velocity from the free stream value to nearly zero at the substrate. (The velocity is not identically zero at the surface due to the net flux of mass onto the substrate.) Because the gas velocity is large and little homogeneous H recombination chemistry takes place, the temperature remains essentially constant at T_{out} in the free stream until the gas gets close to the substrate; it then drops rapidly to the controlled substrate temperature T_s. Energy transport within the boundary layer is dominated by diffusion, and the temperature varies nearly linearly with distance, as shown in Fig. 5. Although [H] remains nearly constant in the free stream,
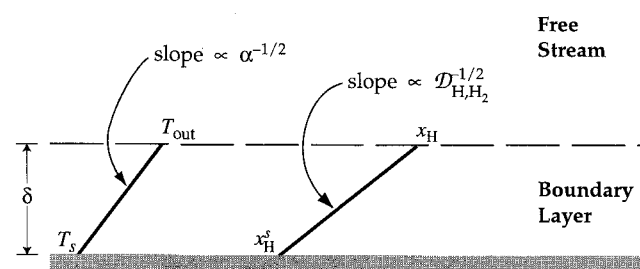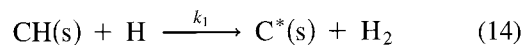

FIG. 5. Diagram of the boundary-layer region. In this region, temperature and [H] both drop sharply from their free stream values.

reactions on the diamond surface efficiently remove H from the gas phase. The sharp drop in H concentration between the free stream and the surface is due to its participation in two reactions,

$$CH(s) + H \xrightarrow{\ k_1\ } C^*(s) + H_2 \qquad (14)$$

$$C^*(s) + H \xrightarrow{\ k_2\ } CH(s) \qquad (15)$$

There are other surface reactions occurring and other surface species present beside $CH(s)$ and $C^*(s)$, as discussed in the next section, but the reactions in (14) and (15) dominate and these two species also dominate. The slow rate of homogeneous H recombination and small effect on H concentration of gas-phase reactions of H with hydrocarbons give rise to a linear variation of atomic hydrogen mole fraction with distance. The atomic hydrogen profile in the boundary layer is also depicted in Fig. 5.

Hydrodynamic theory provides a means of predicting the thicknesses of the three boundary layers present at the surface. The thicknesses of the momentum, thermal, and atomic hydrogen boundary layers, denoted as δ_v, δ_T, and δ_H, respectively can be approximated by

$$\delta_v = 2\sqrt{\frac{Lv}{U_\infty}} \quad \delta_T = 2\sqrt{\frac{L\alpha}{U_\infty}} \quad \delta_H = 2\sqrt{\frac{L\mathcal{D}_{H,H_2}}{U_\infty}}. \qquad (16)$$

In Eq. (16), $v = \mu/\rho$ is the kinematic viscosity of the gas mixture, $\alpha = \lambda/(\rho C_p)$ is the mixture thermal diffusivity, and $\mathcal{D}_{H,H_2}$ is the binary diffusion coefficient of H in H_2; L is a characteristic reactor length scale, as described at the beginning of the section. Strictly speaking, the atomic hydrogen boundary-layer thickness depends on the mixture diffusion coefficient for H, $\mathcal{D}_{H,m}$, but since H_2 is present is such large quantity relative to all other species in the system, $\mathcal{D}_{H,m} \approx \mathcal{D}_{H,H_2}$. Thus, given knowledge of the flow rate of H_2 passing though the plasma torch (this quantity is solved for in the plasma torch model), and the temperature and pressure of the gas in the free stream, it is possible to obtain an *a priori* estimate of the boundary-layer thicknesses in the arcjet reactor. As with many gaseous systems, the three boundary-layer thicknesses are comparable in magnitude because the Schmidt (Sc $= v/\mathcal{D}_{H,H_2}$) and Lewis (Le $= \alpha/\mathcal{D}_{H,H_2}$) numbers are not too far removed from unity.[14] For conditions considered here, Sc ≈ 0.55, Le ≈ 0.76, and thus $\delta_v/\delta_H \approx 0.75$ and $\delta_T/\delta_H \approx 0.9$.

Once values of δ_T and δ_H are known it is possible to obtain accurate predictions for the heat and atomic hydrogen fluxes to the surface. Assuming that diffusive transport of energy and mass dominate convective transport in the boundary layer (a reasonable assumption in these systems because growth rate is so slow, and Stefan velocity at the surface is orders of magnitude smaller than the free stream velocity), it's possible to obtain

analytical expressions for these two fluxes. The heat flux to the surface is

$$q_0 = -\lambda \frac{dT}{dz}\bigg|_{z=0} \equiv -\lambda \frac{T_{\text{out}} - T_s}{\delta_T}, \qquad (17)$$

where λ is the thermal conductivity of the gas mixture. The difference expression on the right-hand side of (17) is an identity if the temperature profile in the boundary layer is linear and the thermal conductivity is constant. Similarly, the molar flux of atomic hydrogen to the substrate is given by

$$N_{H_0} = -c\mathcal{D}_{H,H_2} \frac{dx_H}{dz}\bigg|_{z=0} \equiv -c\mathcal{D}_{H,H_2} \frac{x_H - x_H^s}{\delta_H}, \qquad (18)$$

where c is the mixture concentration. Again, the finite difference expression on the right-hand side of (18) is an identity if the atomic hydrogen mole fraction profile is linear in the boundary layer. In (17) and (18) the transport properties, λ and $c\mathcal{D}_{H,H_2}$, are evaluated at the midpoints of the thermal and concentration boundary layers in this simplified treatment. [These parameters are evaluated at the midpoint because the expressions in (17) and (18) are equivalent to second-order, centered finite difference approximations for the derivatives.] Because there is no net accumulation of gas-phase H at the surface, a mass balance at the surface provides a link between the flux of H to the surface and its rate of disappearance due to Eqs. (14) and (15):

$$N_{H_0} = -k_1[CH(s)][H] - k_2[C^*(s)][H]. \qquad (19)$$

Assuming the surface is at steady state, the concentrations of the two surface species can be related to one another,

$$[C^*(s)] = \frac{k_1}{k_2}[CH(s)], \qquad (20)$$

and to the total site density Γ, such that $[C^*(s)] \approx \Gamma - [CH(s)]$. The relationships among $[CH(s)]$, $[C^*(s)]$, and

Γ can be substituted into Eq. (19) to yield

$$N_{H_0} = -\frac{2k_1k_2}{k_1 + k_2}\Gamma[H] = -\frac{2k_1k_2}{k_1 + k_2}\Gamma c x_H^s, \qquad (21)$$

where c is the total concentration of all gas-phase species, and x_H^s represents the gas-phase mole fraction of H at the substrate. Finally, equating (21) and (18), an expression describing the drop in atomic hydrogen mole fraction across the boundary layer is obtained:

$$\frac{x_H}{x_H^s} = 1 + \frac{2k_1k_2}{k_1 + k_2}\frac{\Gamma\delta_H}{\mathcal{D}_{H,H_2}},$$

or,

$$\frac{x_H^s}{x_H} = \frac{1}{1 + \text{Da}_{\text{eff}}}, \qquad (22)$$

where

$$\text{Da}_{\text{eff}} = \frac{2k_1k_2}{k_1 + k_2}\frac{\Gamma\delta_H}{\mathcal{D}_{H,H_2}} \qquad (23)$$

is the effective Damköhler number for atomic hydrogen in this system.[8] This dimensionless parameter provides a measure of the ratio of the rate of destruction of H at the surface by heterogeneous reaction to the rate of delivery of H to the surface by mass diffusion. For $\text{Da}_{\text{eff}} \gg 1$, mass transfer cannot keep up with the rate at which H reacts with the surface and the system becomes mass-transfer limited. Conversely, when $\text{Da}_{\text{eff}} \ll 1$ the surface reactions (14) and (15) are slow relative to the rate at which H diffuses to the surface, and the system becomes kinetics limited.

The expressions in (17) and (18) have been applied to predict the fluxes of heat and atomic hydrogen to the surface for four different operating conditions, and these have been tabulated with results obtained from a stagnation flow model, SPIN, as shown in Table I. Values of Da_{eff} from Eq. (23) are also listed in the table; as can be seen, even in a highly convective reactor such as the one modeled here, the system is slightly

TABLE I. Predicted values of boundary-layer thicknesses and atomic hydrogen flux and heat flux to the substrate from the full stagnation flow model (SPIN)[12] and the model developed in the current work; and predicted values of the effective Damköhler number for H atom loss. Full profiles for these cases are shown in Fig. 7.

		Boundary-layer thickness		Predicted flux to substrate		
		δ_H (cm)	δ_T (cm)	H (g cm^{-2} s^{-1})	Heat (W cm^{-2})	Da$_{\text{eff}}$
30 Torr, 2500 K,	SPIN	0.39	0.32	1.35×10^{-4}	39.1	$\cdots$
0.1% CH$_4$	Present work	0.41	0.35	1.48×10^{-4}	39.3	5.3
30 Torr, 2500 K,	SPIN	0.43	0.32	1.17×10^{-4}	39.4	$\cdots$
1.1% CH$_4$	Prsent work	0.41	0.35	1.33×10^{-4}	39.5	5.3
10 Torr, 2500 K,	SPIN	0.60	0.50	8.13×10^{-5}	27.8	$\cdots$
0.1% CH$_4$	Present work	0.60	0.51	8.37×10^{-5}	27.2	2.6
30 Torr, 3000 K,	SPIN	0.38	0.33	5.98×10^{-5}	67.4	$\cdots$
0.1% CH$_4$	Present work	0.37	0.31	6.11×10^{-5}	66.5	3.8

mass-transfer limited in atomic hydrogen, although not to as great an extent as in hot-filament, microwave, or atmospheric combustion systems. The thermal and concentration boundary-layer thicknesses appearing in (17) and (18) were computed using Eq. (16). The boundary-layer thicknesses for the SPIN calculations were taken to be the distance over which temperature or H mole fraction rose from their surface values to 95% of the free stream values.

For the four cases listed in Table I, a 25 kW plasma torch was employed, and conditions were chosen such that reactor pressure, inlet CH_4 fraction, and H fraction were independently varied. The conditions corresponding to each case are listed in the table and in the caption of Fig. 7. Representative temperature profiles in the vicinity of the surface from the analytical model and calculated by SPIN are shown in Fig. 6, corresponding to the conditions in the first two lines of Table I and in Fig. 7(a). While the slopes of the temperature profiles shown in Fig. 6 are different, the predicted heat fluxes are nevertheless very close to one another. The explanation is that, although the slope of the approximate temperature profile is less than that predicted by SPIN within the boundary layer, the thermal conductivity appearing in Eq. (17) is evaluated at the boundary-layer midpoint, the heat flux predicted by SPIN, utilizing an expression analogous to Eq. (17), involves transport properties evaluated at the surface conditions. In other words, the slope of the SPIN temperature profile is higher, but its thermal conductivity is lower because it

is evaluated at the surface temperature. For the same reason, the predicted flux of H from Eq. (18) is close to that predicted by the stagnation flow model, even though the slope of the atomic hydrogen profile appearing in Eq. (18) is less than that predicted by the exact result.

The surface reactions involving gas-phase hydrocarbon species such as CH_3 and C do not proceed at a sufficiently fast rate to affect the concentrations of these species, but the gas-phase hydrocarbon species distributions *are* strongly affected by the drop in [H] through the boundary layer and the drop in temperature. The reduction in atomic hydrogen drives the reactions in Eq. (10) to the left, with the reverse rates increasing to 4–8 times those of the forward rates. Although the constantly changing H concentration with position in the boundary layer prevents the C1 species from reaching partial equilibrium, the rapidity of the H addition reactions in Eq. (10), coupled with the finite diffusion time ($\approx 25-50$ μs), nevertheless can result in appreciable changes to the C1 species distributions within this small spatial region. Thus the effects of both finite-rate homogeneous chemistry and transport must be accounted for within the boundary layer.

Stagnation flow calculations[4,5] demonstrate that the C1 species mole fraction profiles in arcjet systems are well fit by an expression of the form $x_i = A_i + B_i e^{-C_i z}$, where A_i, B_i, and C_i are constants, i refers to each C1 species, and $z = 0$ corresponds to the surface. But because $\delta_H \ll L$, a Taylor series expansion of these expressions can be truncated after two terms so that close to the surface (within the boundary layer) the C1 mole fraction profiles are nearly linear:

$$x_i \approx (A_i + B_i) - B_i C_i z + \text{H.O.T.}$$
$$(i = CH_4, CH_3, CH_2, CH, C). \qquad (24)$$

Neglecting the effect of convection on hydrocarbon species transport in the boundary layer, and taking advantage of the nearly linear profiles of these species, a one-dimensional species conversation equation can be written for each of the five C1 species plus C_2H_2,

$$0 = \frac{M_{H_2}}{M} \frac{d}{dz}\left(c\mathcal{D}_{i,H_2} \frac{dx_i}{dz}\right)$$
$$+ \frac{M_{H_2}}{M} \frac{d}{dz}\left(c\mathcal{D}_{i,H_2} k_{T_i} \frac{d}{dz} \ln T\right) + \dot{\omega}_i$$
$$= \frac{M_{H_2}}{M} \frac{dx_i}{dz} \frac{d}{dz}(c\mathcal{D}_{i,H_2})$$
$$+ \frac{M_{H_2}}{M} \frac{d}{dz}\left(c\mathcal{D}_{i,H_2} k_{T_i} \frac{d}{dz} \ln T\right) + \dot{\omega}_i, \qquad (25)$$

where $\dot{\omega}_i$ is the instantaneous volumetric molar production rate of species i to the reactions in
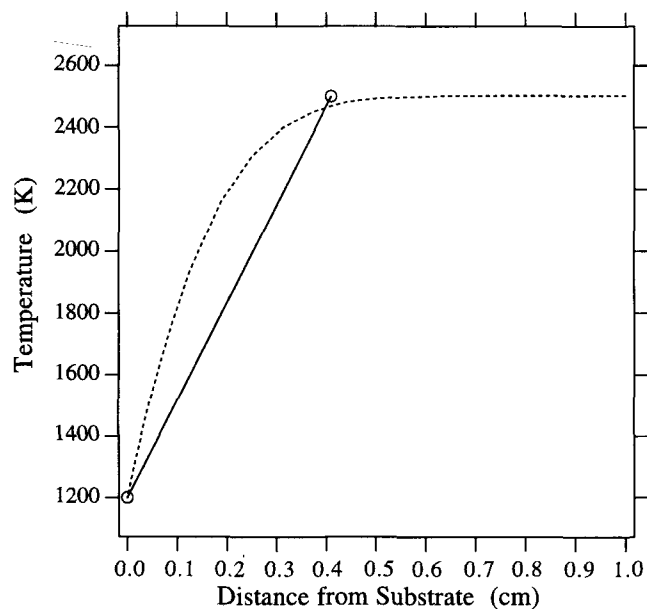

FIG. 6. A representative temperature profile in the vicinity of the surface, corresponding to the conditions in Fig. 7(a). The dashed line represents the SPIN calculation, while the solid line joins the free stream and surface temperatures.
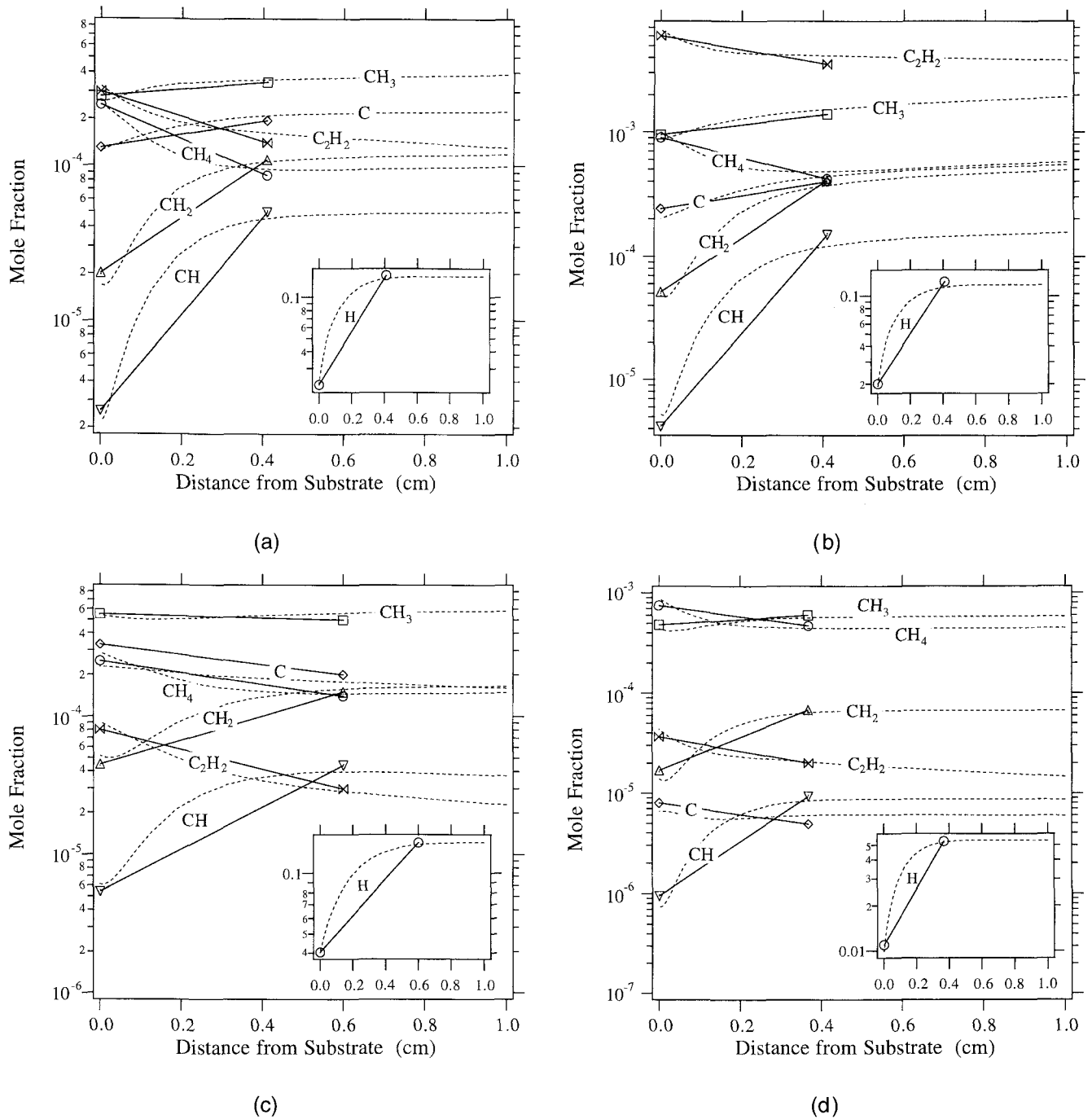
(a)

(b)

(c)

(d)

FIG. 7. Comparison of detailed stagnation flow calculations (dashed lines) and the results from the model developed in this work (symbols). The straight solid lines join the adjusted equilibrium values at the boundary-layer edge with the values predicted at the surface. (a) $p = 30$ Torr, $T_{out} = 2500$ K, 0.1% CH_4 at inlet; (b) $p = 30$ Torr, $T_{out} = 2500$ K, 1.1% CH_4 at inlet; (c) $p = 10$ Torr, $T_{out} = 2500$ K, 0.1% CH_4 at inlet; (d) $p = 30$ Torr, $T_{out} = 3000$ K, 0.1% CH_4 at inlet.

Eq. (10), M is the number mean molecular weight of the mixture, and $\mathcal{D}_{i,H_2}$ and k_{T_i} are the binary diffusion coefficient and thermal diffusion ratio, respectively, for i in H_2 (assuming that H_2 is present in great excess relative to all other gas-phase species). The term $\dot{\omega}_{C_2H_2}$ in the conservation equation for C_2H_2 is set to zero in this formulation because the C1 species are attempting to

rapidly rearrange around the local atomic hydrogen concentration, and the rate of formation of C2 species through bimolecular reactions is low. This assumption is not strictly rigorous, but is a reasonable approximation for the range of hydrocarbon and atomic hydrogen concentrations studied here. Experience gained in simulating dc arcjet systems indicates that thermal diffusion

can contribute significantly to diffusive transport of the hydrocarbon species within the boundary layer, and this effect cannot in general be neglected. Equation (25) is evaluated at the surface, and one-sided, second-order accurate finite difference approximations are employed for the two first derivatives in the first term. The Soret diffusion flux term for each of the species is a function of not only the local temperature gradient and pressure, but also the relative amounts of each species and H_2. However, because the mole fraction of each C1 species and C_2H_2 is generally less than 1%, the effect of varying C1 and C_2H_2 mole fractions in the boundary layer has a negligible effect on the magnitudes of the thermal diffusion ratios, and k_{T_i} can therefore be evaluated for representative values of x_i and then treated as implicitly known functions of position in the boundary layer. The set of six algebraic equations resulting from Eq. (25) is linear in the six unknown C1 mole fractions and C_2H_2 at the surface, $x^s_{CH_x}$ and $x^s_{C_2H_2}$. The species production rates in Eq. (25) depend on the forward rates of the reactions in Eq. (10), shown in Table II, and the reverse rates which are computed using the free energy changes of the reactions. The linear system can be solved exactly to yield analytical expressions for the mole fractions of the single-carbon species at the surface, $x^s_{CH_x}$, and $x^s_{C_2H_2}$, in terms of their adjusted free stream fractions, x_{CH_x} and $x_{C_2H_2}$, and k_{f_i}, k_{r_i}, δ_H, x^s_H, $x^s_{H_2}$, and the gradients of the quantity $c\mathcal{D}_{i,H_2}$.

The profiles in Figs. 7 illustrate the boundary-layer species profiles resulting from application of Eq. (25); the dashed lines the figures are the profiles predicted by the stagnation flow calculations, including full gas-phase chemistry and transport. The solid lines join the adjusted equilibrium mole fractions predicted using the free stream model in Sec. II.B to the values resulting from the discrete solutions to Eq. (25) for each of the hydrocarbon species. For both the stagnation flow calculations and the simplified model calculations, the arcjet model of Sec. II.A was applied to predict the mass flow rate through the plasma torch and the H:H_2 distribution leaving the torch, given a specified outlet temperature and torch power. For the stagnation flow calculations the torch-substrate separation was chosen

TABLE II. Forward rate constants for the hydrogen abstraction reactions shown in Eq. (10).[11]

	Reaction	A_i[a]	b_i	E_i
G1	$H + CH_4 \rightleftharpoons CH_3 + H_2$	0.22×10^5	3	8,750
G2	$H + CH_3 \rightleftharpoons CH_2 + H_2$	0.9×10^{14}	0	15,100
G3	$H + CH_2 \rightleftharpoons CH + H_2$	0.1×10^{19}	−1.56	0
G4	$H + CH \rightleftharpoons C + H_2$	0.15×10^{15}	0	0

[a] $k_{f_i} = A_i T^{b_i} e^{-E_i/RT}$ (A_i in moles, cubic centimeters, and seconds; E_i in cal/mole).

to be 10 cm, and the stagnation velocity at the torch exit was computed using the mass flow rate and a torch orifice 3 cm in diameter. Methane was introduced into the H–H_2 mixture at the torch exit to produce either 0.1% or 1.1% CH_4 initial concentrations.

Four different cases are presented: Fig. 7(a) represents a nominal set of conditions consistent with calculations done previously,[5] with a reactor pressure of 30 Torr, a torch outlet temperature of 2500 K, and 0.1% CH_4 at the inlet; in Fig. 7(b) the inlet CH_4 has been increased tenfold over Fig. 7(a), to 1.1%; the conditions in Fig. 7(c) are the same as in 7(a), except that the reactor pressure has been decreased to 10 Torr; and in Fig. 7(d) the conditions have been modified so that the outlet gas temperature is 3000 K, lowering the amount of H produced in the torch, and downstream H_2 has been introduced, further lowering the free stream [H] from 15% in Figs. 7(a)–7(c) to 5% in Fig. 7(d). The intent of the four plots in Fig. 7 is to investigate the validity of applying the simplified model to a range of inlet CH_4 mole fractions, reactor pressures, and H_2 dissociation fractions. In all four cases the torch power was set at 25 kW. The boundary-layer thicknesses shown in Figs. 7(a)–7(d), that is, the distances on the abscissa over which the mole fractions change according to the simplified model, are predicted using Eq. (16) and shown in Table I. As can be seen from each of the four plots in Fig. 7, the overall agreement between the simplified model and the detailed stagnation calculations is sufficiently good to validate the simplified model.

As with the temperature profile shown in Fig. 6, the actual slopes of the H atom profiles at the surface shown in Fig. 7 are different from the slopes resulting from Eq. (18), even though x^s_H and the predicted H atom fluxes at the surface match closely. Because the quantity $c\mathcal{D}_{H,H_2}$ is evaluated at the midpoint of the boundary layer, the H profiles denoted by the solid lines in Fig. 7 reflect the average slope of the actual H profile. While the results of Eqs. (18)–(22) can be used to predict the drop in H through the boundary layer and subsequent flux of H at the deposition surface, the fluxes of the hydrocarbon species at the surface cannot be extracted from the reduced conservation equation written in Eq. (25). The drop in H through the boundary layer and resulting slope at the surface is driven solely by heterogeneous chemistry; the change in hydrocarbon mole fractions through the boundary layer is in response to the change in local [H], and the approximate or average slopes of these profiles are not necessary linked to their fluxes at the surface. In reality, the true slope of each profile of hydrocarbon species at the surface is linked to its flux, and this behavior is reflected by the dashed lines in Figs. 7(a)–7(d): the overall slopes of the hydrocarbon mole fractions through the entire boundary layer from Eq. (25) follow the SPIN results, but the true slope of

each hydrocarbon at the surface is determined by the reactivity of that species with the diamond surface, and the adjustment in slope occurs over a spatial distance much smaller than even the boundary-layer thickness. Thus, the simplified model can be used to predict the change in each hydrocarbon species between the plasma torch exit and the deposition surface, but only the fluxes of energy and atomic hydrogen are computed via this transport analysis. However, it is still possible to calculate the diamond growth rate, which is done in the next section.

D. Deposition chemistry

Much theoretical analysis has been done on the elementary heterogeneous chemical reactions leading to diamond deposition. There will likely never be full agreement on the details of the process. However, it has been found that relatively few reactions are needed if the goal is limited to an accurate description of deposition rates. In the spirit of the foregoing discussion, we use the simplest possible reaction mechanism in our reactor model which still captures the features of interest. Specifically, earlier modeling work showed that CH_3, atomic C, or a combination of the two could be responsible for bringing carbon to the surface in dc arcjet systems, depending on reaction conditions. It has also observed that, depending upon growth conditions, point defects are incorporated into the lattice.

Goodwin has given a simplified set of surface reactions that can describe diamond growth rates over a wide range of conditions.[7] The reactions in his simplified mechanism are listed as numbers S1 through S6 in Table III. The four surface species listed in Table III are $CH(s)$, a surface carbon bonded to a hydrogen; $C^*(s)$, a surface carbon with one dangling bond, i.e., a radical site; $CM(s)$, a CH_3 bonded to a surface carbon atom; and $CM^*(s)$, a CH_2 group bonded to a surface carbon, which also has one dangling bond. Two bulk species are

TABLE III. Surface reaction mechanism describing the growth of diamond, D, and the formation of buried point defects, P_d, from C and CH_3 precursors.

Number	Reaction	k_i[a]
S1	$CH(s) + H \longrightarrow C^*(s) + H_2$	2.9×10^{12}
S2	$C^*(s) + H \longrightarrow CH(s)$	1.7×10^{13}
S3	$C^*(s) + CH_3 \longrightarrow CM(s)$	3.3×10^{12}
S4	$CM(s) \longrightarrow C^*(s) + CH_3$	1.0×10^4
S5	$CM(s) + H \longrightarrow CM^*(s) + H_2$	2.0×10^{12}
S6	$CM^*(s) + H \longrightarrow CH(s) + H_2 + D$	4.0×10^{13}
S7	$C^*(s) + C \longrightarrow C^*(s) + D$	3.3×10^{12}
S8	$CM^*(s) + CH_3 \longrightarrow CM(s) + P_d + H_2$	7.5×10^8
S9	$CM^*(s) + C \longrightarrow C^*(s) + P_d + D + H_2$	7.5×10^8

[a]k_i in moles, cubic centimeters, and seconds; valid at 1200 K.

included in Table III, a diamond lattice atom D, and a lattice point defect P_d. A simplified set of reactions, such as listed in Table III, is not intended to be mechanistically correct in its detail, but just to capture the main features of the CVD process. Describing the process through such a sequence of "generic" steps also allows one to estimate reasonable rate constants and activation energies for use in a kinetic simulation.

Goodwin provides rate constants for reactions S1–S5 (at 1200 K), which were set to match rates from a variety of H-recombination experiments, molecular dynamics simulations, an empirical fit to deposition rates predicted by the more detailed deposition mechanism of Harris,[15] and to give an average lifetime of 100 μs for surface CH_3.[7] (The rate constant for reaction S6 was not given explicitly by Goodwin, but was listed as "fast." At steady state, the deposition rate is independent of this rate constant, and so we have supplied a value sufficiently "fast" for the simulations). As in the mechanism presented by Goodwin, activation energies are not supplied for this simplified heterogeneous kinetics model—it is intended to be valid within some small range of 1200 K. The model was tested with 7300 cal/mole activation energies for the H-abstraction reactions (S1, S5, S6),[16] and with the CH_3 desorption (S4) activation energy set to our earlier estimate of the bond strength.[5] With activation energies present the model was in quantitative agreement with experiment regarding the existence of a maximum growth rate with T_s (≈ 1150 K).[17–19] However, the model did not correctly capture the observed 20 kcal/mole effective activation energy for growth for $T_s < 1150$ K[18,19]; the predicted activation energy was approximately 10 kcal/mole too low.

Reaction S7 was included to account for deposition from C-atoms. Earlier modeling studies of the dc arcjet deposition system show that under certain conditions (high H_2-dissociation fractions) C was the most abundant carbon-containing species in the gas.[5,6] Because C is a very reactive species, its contribution to the diamond deposition should not be neglected. The rate constant for S7 was set equal to that of reaction S3. Goodwin has pointed out[7] that reactions S1 through S6 do a good job of reproducing measured growth rates over a wide range of conditions. For conditions typical of the dc arcjet reactor, Fig. 8 shows that the diamond growth rate scales linearly with CH_3 mole fraction at the surface using the set of reactions in Table III.

Under conditions of high growth rate, defects can be incorporated into the diamond lattice. Such defects could be sp^2 in nature, formed via a β-bond cleavage from unimolecular decomposition of adjacent $C^*(s)$ and $CH(s)$ species; Butler and Woodin[20] present a simple kinetic analysis for growth of this type of defect. They also discuss sp^3 defects, characterized by hydrogen bonded
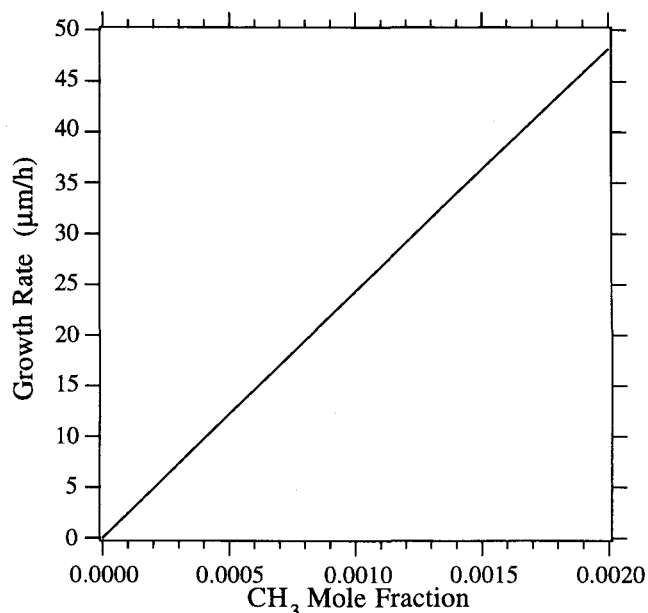
FIG. 8. Diamond growth rate as a function of CH_3 mole fraction using the mechanism from Table II. Other conditions for the calculation: H mole fraction = 0.02, with the remainder of the gas H_2, 20 Torr total pressure, surface temperature 1200 K.

to sp^3 carbons, in which subsequent layers of carbon add to the surface before all of the surface hydrogen atoms have been displaced through H-abstraction and C–C bond formation reactions.[20] However, no specific kinetic scheme was suggested for formation of these defects.

Reactions S8 and S9 have been included in our reduced surface reaction mechanism in Table III to describe "over growth" of an sp^3 defect, trapping hydrogen into the lattice. Although not to be considered elementary reactions, S8 and S9 should nonetheless capture the important features. These reactions involve a reactive carbon species (either CH_3 or C) reacting with the $CM^*(s)$ species, as a competition to the diamond growth reaction of $CM^*(s)$, reaction S6. Thus, reactions S8 and S9 will be important under conditions of high growth rate when the concentration of carbon species becomes larger relative to gas-phase H.

A few comments about the form of reactions S8 and S9 are in order. First, Butler and Woodin[20] include a reaction similar to S8 (except forming a surface C_2H_5 species) as part of a proposed mechanism for normal diamond growth on the (110) surface. Thus, a reminder that the reactions in Table III have to be considered generic rather than elementary. Second, note that S8 and S9 are first-order in the surface reactant $CM^*(s)$. We will make comments later about the scaling of lattice-defect formation rates with respect to the reaction order of their creation. Finally, rate constant information is not available for reactions S8 and S9. The value given

in Table III was set to yield defect densities in the parts-per-million range, consistent with EPR measurements.[21] For purposes of the next discussion, the set of reactions S1–S9 will be referred to as M1 (mechanism 1).

Goodwin[7] also included arguments concerning the scaling of defect formation with process conditions. The basic assumption in that work was that defects were formed by reaction of a surface adsorbate with a nearby adsorbate before it had been fully incorporated into the lattice. However, a precise chemical reaction for forming the defect was not mentioned. This simple picture is similar in spirit to the Butler and Woodin[20] picture of sp^3 defect formation just mentioned. The assumption that the defect formation reaction was second-order in surface reactants led to a simple scaling relationship[7] between defect fraction X_d, growth rate, G, and hydrogen-atom molar concentration [H]:

$$X_d \propto \frac{G}{[\mathrm{H}]^2}. \tag{26}$$

Goodwin was careful to point out the exact form of the scaling of defect formation is uncertain, and that Eq. (26) would more generally be written with an exponent n in the denominator, where n is determined experimentally.

We note that scaling of defect fraction rate depends upon the order of the surface reaction forming the defect. This is illustrated by comparing scaling of the reaction set M1 with predictions using a defect-formation reaction second order in the surface adsorbate, such as

$$2\,CM(s) \longrightarrow CM(s) + CH(s) + H_2 + P_d. \tag{S10}$$

The precise form of such a second order reaction, especially the list of products, is uncertain. However, reaction S10 will suffice for the current purpose, which is examining the dependence of defect formation scaling with respect to the order of the surface reaction. For this example, the rate constant for S10 was set to 3.0×10^8; this value was chosen to give roughly the same defect formation rates as reaction set M1 for a nominal arcjet condition with H-atom mole fraction of 0.02 and CH_3 mole fraction of 0.001. The set of reactions S1–S7 and S10 will be denoted M2.

Figure 9 shows that, for a fixed concentration of H at the surface, the lattice defect fraction increases linearly with CH_3 concentration at the surface for both sets of reactions M1 and M2. (Here the defect fraction is taken to be the ratio of the defect growth rate to the diamond growth rate.) The defect fraction will also scale linearly with C-atom concentration at the surface for set M1, but for simplicity of discussion is not plotted. Since growth rate and defect fraction both increase linearly with CH_3 fraction, it is immediately clear that defect fraction will increase (and diamond "quality" will decrease) as growth rate increases for either set of reactions.
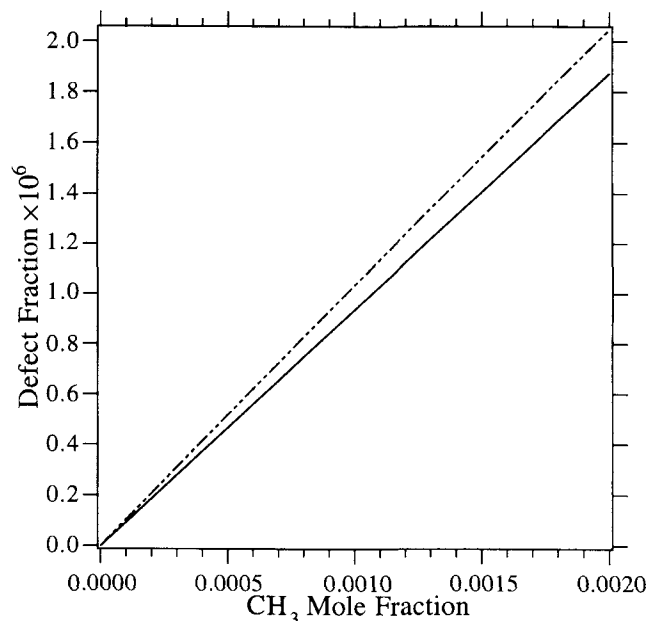
FIG. 9. Calculated defect mole fraction as a function of CH_3 mole fraction using reaction sets M1 (solid line) and M2 (dashed line). See text for definition of reaction sets. Other conditions are the same as in Fig. 8.

The diamond growth rate attainable for a fixed defect density scales differently for the two sets of reactions M1 and M2, as illustrated in Fig. 10. For this plot, defect density was specified to be 10^{-6} mole fraction, and for each value of [H], the amount of CH_3 necessary to attain that defect fraction was determined; the allowable CH_3 mole fraction at fixed density as a function of [H] is shown in Fig. 11. For larger values of [H], Fig. 10 shows that set M1 predicts the growth rate at fixed defect density will scale approximately linearly with H concentration. For reaction set M2, the attainable growth rate at fixed defect density scales quadratically with [H]; this is consistent with the formula given by Goodwin,[7] Eq. (26). For the defect mechanism that includes the first-order (in surface adsorbate) reactions, set M1, the allowable CH_3 increases linearly with H concentration (solid curve in Fig. 11). For reaction set M2, which includes the second-order defect formation reaction S10, the allowable CH_3 increases quadratically with H (dashed curve in Fig. 11).

The difference in scaling of growth rate with H-atoms at constant defect density has implications for making higher powered arcjet reactors. If defect formation scales as in the first-order reaction set M1, then increasing the arcjet power would increase H-atom production, giving approximately a linear increase in attainable growth rate. However, if the defect formation is second order in surface adsorbates as in set M2, growth rate at constant quality increases quadratically

with [H], indicating much larger pay-off in going to higher power (higher H_2 dissociation fraction).

III. CONCLUSION

A simplified model has been presented whereby diamond growth rate and defect formation rate in dc arc-jet reactors may be computed, requiring only specification of torch power, free stream gas temperature, reactor pressure, CH_4 injection rate, downstream H_2 injection rate (if any), substrate temperature, and torch-substrate separation distance. While the model was presented for pure H_2 feed into the plasma torch, it can readily be adapted for the inclusion of an additional gas, such as argon. Also, the torch model in Sec. II. A was based on the presumption that torch power and free stream temperature were known. However, Gibbs phase rule indicates that for the plasma torch, two constrains must be imposed to specify the state of the system, thus, two degrees of freedom other than those employed here could be used, for example, torch power and inlet H_2 flow rate.

The model developed in this work has been tested against detailed stagnation flow calculations, which in turn have been compared with experiment where possible.[5] The simplified model has proven to yield results consistent with those from stagnation flow models for $5 \leq P \leq 60$ Torr and $2000 \leq T_{out} \leq 3500$ K. For pressures lower than approximately 5 Torr the free stream jet is supersonic, and cannot be approximated
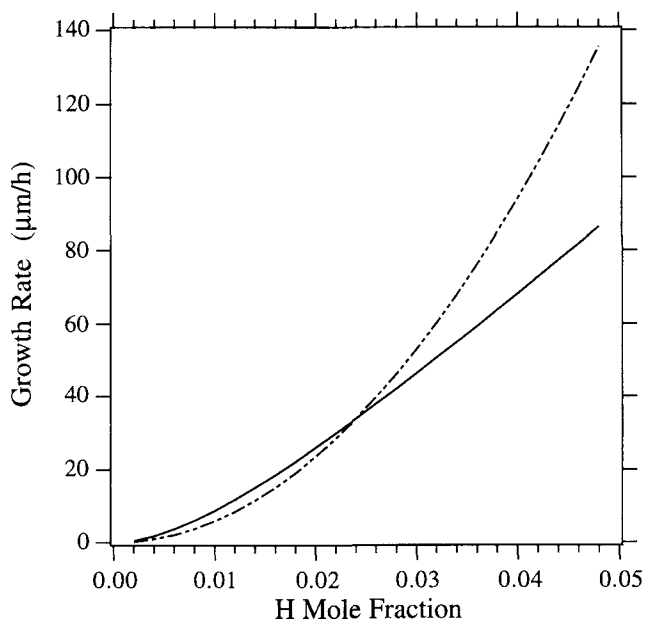

FIG. 10. Growth rate as a function of gas-phase H mole fraction obtained for a fixed defect mole fraction of 10^{-6} using reaction sets M1 (solid line) and M2 (dashed line). The CH_3 concentration was adjusted to obtain the desired defect fraction (see Fig. 9). Other conditions are the same as in Fig. 8.
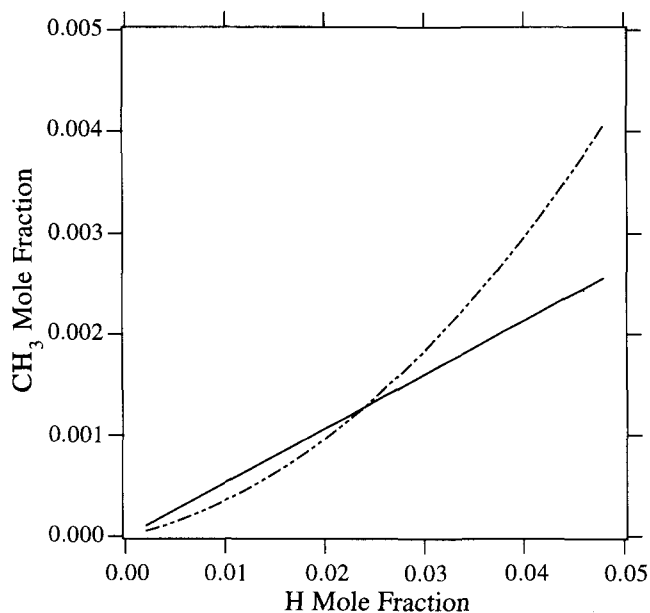
FIG. 11. CH_3 mole fraction needed to obtain a growth rate at constant defect density of 10^{-6} as a function of gas-phase H mole fraction. Other conditions are the same as in Fig. 8.

by the laminar flow assumptions imposed here; for pressures above 60 Torr appreciable homogeneous H recombination occurs, and the free stream and boundary-layer models would have to be modified to account for this chemistry. Temperatures outside the range given above were not examined in this work.

ACKNOWLEDGMENTS

REFERENCES

1. F. M. Cerio and W. A. Weimer, Rev. Sci. Instrum. **63**, 2065 (1992).
2. R. L. Woodin, L. K. Bigelow, and G. L. Cann, Proceedings of *Applications of Diamond Films and Related Materials* (Auburn, AL, 1991), p. 439.
3. L. Rongzhi, S. Hailiang, Y. Zhen, T. Sen, and Z. Hesun, Proceedings of *Applications of Diamond Films and Related Materials* (Auburn, AL, 1991), p. 207.
4. D. G. Goodwin, Appl. Phys. Lett. **59**, 277 (1991).
5. M. E. Coltrin and D. S. Dandy, J. Appl. Phys. **74**, 5803 (1993).
6. B. W. Yu and S. L. Girshick, J. Appl. Phys. **75**, 3914 (1994).
7. D. G. Goodwin, J. Appl. Phys. **74**, 6888 (1993).
8. D. G. Godwin, J. Appl. Phys. **74**, 6895 (1993).
9. R. M. Young, Surf. Coat. Technol. **68/69**, 384 (1994).
10. S. I. Sandler, *Chemical and Engineering Thermodynamics*, 2nd ed. (John Wiley & Sons, New York, 1989).
11. J. A. Miller and C. F. Melius, Combust. Flame **91**, 21 (1992).
12. M. E. Coltrin, R. J. Kee, G. H. Evans, E. Meeks, D. S. Dandy, F. Rupley, and J. F. Grcar, "SPIN: a Fortran program for modeling one-dimensional rotating-disk/stagnation-flow chemical vapor deposition reactors," Report No. SAND91-8003 (1991).
13. M. Frenklach, H. Wang, C. T. Bowman, R. K. Hanson, G. P. Smith, D. M. Golden, W. C. Gardiner, and V. Lissianski, Proceedings of *25th International Symposium on Combustion* (Irvine, CA, 1994), poster presentation.
14. D. E. Rosner, *Transport Processes in Chemically Reacting Flow Systems* (Butterworths, Boston, MA, 1986).
15. S. J. Harris, Appl. Phys. Lett. **56**, 2298 (1990).
16. C. K. Westbrook, J. Warnatz, and W. J. Pitz, Proceedings of *Twenty-second Symposium (International) on Combustion* (Seattle, WA, 1988), p. 893.
17. E. Kondoh, T. Ohta, T. Mitomo, and K. Ohtsuka, Appl. Phys. Lett. **59**, 488 (1991).
18. E. Kondoh, T. Ohta, T. Mitomo, and K. Ohtsuka, J. Appl. Phys. **73**, 3041 (1993).
19. S. J. Harris and A. M. Weiner, J. Appl. Phys. **75**, 5026 (1994).
20. J. E. Butler and R. L. Woodin, Philos. Trans. R. Soc. **342**, 209 (1993).
21. M. E. Newton, A. Cox, and J. M. Baker, personal communication (1994).
22. J. O. Hirschfelder, C. F. Curtiss, and R. B. Bird, *Molecular Theory of Gases and Liquids*, 1st ed. (John Wiley and Sons, New York, 1954), Vol. 1.
23. K. E. Grew and T. L. Ibbs, *Thermal Diffusion in Gases* (Cambridge University Press, Cambridge, 1952).
24. J. Warnatz, in *Numerical Methods in Flame Propagation*, edited by N. Peters and J. Warnatz (Friedr. Vieweg and Sohn, Wiesbaden, 1982).
25. C. C. Brau and R. M. Jonkman, J. Chem. Phys. **52**, 477 (1970).
26. S. Mathur, P. K, Tondon, and S. C. Saxena, Molec. Phys. **12**, 569 (1967).
27. R. J. Kee, G. Dixon-Lewis, J. Warnatz, M. E. Coltrin, and J. A. Miller, "A Fortran computer code package for the evaluation of gas-phase multicomponent transport properties," Report No. SAND86-8246 (1986).

APPENDIX: EVALUATION OF TRANSPORT PROPERTIES

Because dc arcjet systems are typically operated with one gas-phase species present in great excess relative to all others, transport properties used in the evaluation of energy and mass fluxes at the deposition surface, and in the C1 species and C_2H_2 conservation equations in the boundary layer, can be computed using relatively simple binary transport theory. The quantities needed in the reactor model presented in this work include the binary diffusion coefficients of H, C, CH, CH_2, CH_3, CH_4, and C_2H_2 in H_2; the thermal conductivity of an H/H_2 mixture; and the thermal diffusion ratios of C, CH, CH_2, CH_3, CH_4, and C_2H_2. Note that, while it has been assumed H_2 is the major species in the arcjet system, the same analysis would hold for a different major species such as Ar.

J. Mater. Res., Vol. 10, No. 8, Aug 1995

2007

A. Binary diffusion coefficients

The Chapman–Enskog kinetic theory is used to describe the diffusion coefficient for a binary gas mixture:[22]

$$\mathcal{D}_{1,2} = 1.8583 \times 10^{-3} \frac{\sqrt{T^3(M_1 + M_2)/M_1M_2}}{p\sigma_{12}^2\Omega_{12}^{(1,1)}}, \quad (A1)$$

in which $\mathcal{D}_{1,2}$ is in cm^2/s, M is the molecular weight, the temperature T is in Kelvin, pressure p is in atm, σ_{12} is a combined Lennard–Jones parameter specified in Å and defined in terms of the individual species parameters as $\sigma_{12} = 1/2 \ (\sigma_1 + \sigma_2)$, and $\Omega_{12}^{(1,1)}$ is a dimensionless collision function that depends on the reduced temperature, kT/ϵ_{12}. The Lennard–Jones parameter ϵ_{12} is defined in terms of the individual species parameters as $\epsilon_{12} = \sqrt{\epsilon_1\epsilon_2}$.

B. Thermal diffusion ratio

To treat the gas mixture in the boundary layer as multicomponent would require that the coefficients of thermal diffusion D_i^T be obtained from rigorous kinetic theory. However, because the transport of each C1 species and C_2H_2 through the boundary layer is treated as a separate two-component system, it is possible to utilize formulae that yield the thermal diffusion ratio k_T for gas pairs. For a binary gas mixture, the first approximation to the thermal diffusion ratio is given by[22,23]

$$k_T = \frac{x_1x_2}{6\lambda_{12}} \frac{x_1S^{(1)} - x_2S^{(2)}}{X_\lambda + Y_\lambda} (6C_{12}^* - 5), \quad (A2)$$

where x_1 and x_2 are the mole fractions of the two species. The dependence of thermal diffusion on molecular mass is captured by $S^{(1)}$ and $S^{(2)}$:

$$S^{(1)} = \frac{M_1 + M_2}{2M_2} \frac{\lambda_{12}}{\lambda_1} - \frac{15}{4A_{12}^*} \frac{M_2 - M_1}{2M_1} - 1$$

$$S^{(2)} = \frac{M_1 + M_2}{2M_1} \frac{\lambda_{12}}{\lambda_2} - \frac{15}{4A_{12}^*} \frac{M_1 - M_2}{2M_2} - 1$$

$$(A3)$$

The other quantities appearing in Eq. (A2) are

$$X_\lambda = \frac{x_1^2}{\lambda_1} + \frac{2x_1x_2}{\lambda_{12}} + \frac{x_2^2}{\lambda_2}$$

$$Y_\lambda = \frac{x_1^2}{\lambda_1} U^{(1)} + \frac{2x_1x_2}{\lambda_{12}} U^{(Y)} + \frac{x_2^2}{\lambda_2} U^{(2)} \quad (A4)$$

where the functions in Y_λ are

$$U^{(1)} = \frac{4}{15} A_{12}^* - \left(\frac{12}{5} B_{12}^* + 1\right) \frac{M_1}{12M_2} + \frac{(M_1 - M_2)^2}{2M_1M_2}$$

$$U^{(2)} = \frac{4}{15} A_{12}^* - \left(\frac{12}{5} B_{12}^* + 1\right) \frac{M_2}{12M_1} + \frac{(M_2 - M_1)^2}{2M_1M_2}$$

and

$$U^{(Y)} = \frac{4}{15} A_{12}^* \frac{(M_1 + M_2)^2}{4M_1M_2} \frac{\lambda_{12}^2}{\lambda_1\lambda_2} - \frac{1}{12}\left(\frac{12}{5} B_{12}^* + 1\right)$$
$$- \frac{5}{32A_{12}^*}\left(\frac{12}{5} B_{12}^* - 5\right) \frac{(M_1 - M_2)^2}{M_1M_2}.$$

The quantities λ_1, λ_2, and λ_{12} are the thermal conductivities for pure monatomic species 1 and 2, and for a binary mixture of monatomic gases 1 and 2, respectively, and are given by

$$\lambda = 8.3224 \times 10^3 \frac{\sqrt{T/M}}{\sigma^2\Omega^{(2,2)}} \quad (A5)$$

$$\lambda_{12} = 5.8848 \times 10^3 \frac{\sqrt{T(M_1 + M_2)/M_1M_2}}{\sigma_{12}^2\Omega_{12}^{(2,2)}}. \quad (A6)$$

In (A5) and (A6), λ is in erg cm^{-1} K^{-1}, T is in Kelvin, σ is in Å, and $\Omega^{(2,2)}$ is a dimensionless function of the reduced temperature kT/ϵ. Finally, there are three combinations of the collision integrals $\Omega^{(i,j)}$ appearing in the expression for thermal diffusion ratio:

$$A_{12}^* = \Omega_{12}^{(2,2)}/\Omega_{12}^{(1,1)}$$

$$B_{12}^* = (5\Omega_{12}^{(1,2)} - 4\Omega_{12}^{(1,3)})/\Omega_{12}^{(1,1)}$$

$$C_{12}^* = \Omega_{12}^{(1,2)}/\Omega_{12}^{(1,1)} \quad (A7)$$

Evaluation of the $\Omega^{(i,j)}$ and A_{12}^*, B_{12}^* and C_{12}^* as functions of the reduced temperature $\overline{T} \equiv kT/\epsilon$ will be discussed below. The Lennard–Jones parameters appearing in Eqs. (A1)–(A7) are listed in Table AI.

In a binary mixture the thermal diffusion ratio k_T is related to the coefficient of thermal diffusion D_i^T by

$$k_T = \frac{\rho}{c^2M_1M_2} \frac{D_1^T}{\mathcal{D}_{1,2}}, \quad (A8)$$

where c, ρ are the total concentration and density of the mixture. Application of full multicomponent theory to the calculation of D_i^T for the limiting case of two components yields the expression for k_T in Eq. (A2), after application of Eq. (A8).

TABLE AI. The Lennard–Jones parameters used in the transport property evaluations.[27]

	C	CH	CH$_2$	CH$_3$	CH$_4$	H	H$_2$	Ar
σ (Å)	3.298	2.750	3.800	3.800	3.746	2.050	2.920	3.330
ϵ/k (K)	71.4	80.0	144.0	144.0	141.4	145.0	38.0	136.5
Z_{rot}	0	0	0	0	13	0	280	0

C. Thermal conductivity

To obtain an estimate for the thermal conductivity of the mixture it is necessary to know the thermal conductivities of the dominant (in concentration) species. The formula in Eq. (A5) is valid only for monatomic species, and can be applied to calculate the thermal conductivity of H, for example. To compute the thermal conductivity of the major species in this system, H_2, it is necessary to take into account the vibrational and rotational degrees of freedom within that molecule. Denoting the thermal conductivity predicted by Eq. (A5) as λ_m, a general expression for the thermal conductivity of a linear polyatomic species is[24]

$$\lambda = \lambda_m\left(1 - \frac{4}{3\pi}\frac{A}{B}\right) + cR\mathcal{D}\left(1 + \frac{2}{\pi}\frac{A}{B}\right) + c\mathcal{D}\left(C_p - \frac{7}{2}R\right). \tag{A9}$$

The quantity $\mathcal{D}$ is the coefficient of self diffusion of the species, given by

$$\mathcal{D} = 2.628 \times 10^{-3}\frac{\sqrt{T^3/M}}{p\sigma^2\Omega^{(1,1)}}, \tag{A10}$$

C_p is the molar heat capacity at constant pressure, and

$$A = \frac{5}{2} - \frac{\rho\mathcal{D}}{\eta}$$

$$B = Z_{\text{rot}} + \frac{2}{\pi}\left(\frac{5}{3} + \frac{\rho\mathcal{D}}{\eta}\right) \tag{A11}$$

where ρ is the density and η is the coefficient of viscosity:

$$\eta = \frac{4}{15}\frac{M}{R}\lambda_m. \tag{A12}$$

The parameter Z_{rot} in Eq. (A11) is the rotational relaxation collision number adjusted for temperature[25]; values of this parameter at 298 K are listed in Table AI.

To obtain an estimate for the mixture-averaged thermal conductivity, a mole fraction weighted combination averaging formula is used[26]:

$$\lambda_{\text{mix}} = \frac{1}{2}\left[\sum_{k=1}^{K} x_k\lambda_k + \left(\sum_{k=1}^{K} x_k/\lambda_k\right)^{-1}\right]. \tag{A13}$$

D. Polynomial fits to collision integrals

The collision integrals $\Omega^{(i,j)}$ appearing in Eqs. (A1)–(A7) have been evaluated using Lennard–Jones intermolecular potentials, and are tabulated as functions of the reduced temperature $\overline{T}$.[22] To utilize these functions in numerical calculation it is convenient to fit them to continuous analytical expressions. It was found here that the dependence of the collision integrals ($\Omega^{(1,1)}$, $\Omega^{(1,2)}$, $\Omega^{(1,3)}$, $\Omega^{(2,2)}$) on reduced temperature are well

TABLE AII. Polynomial coefficients for collision integral curve-fit expression in Eq. (A14).

	$\Omega^{(1,1)}$	$\Omega^{(1,2)}$	$\Omega^{(1,3)}$	$\Omega^{(2,2)}$
a_0	$3.64143296 \times 10^{-1}$	$1.85615591 \times 10^{-1}$	$7.31839709 \times 10^{-2}$	$4.61819834 \times 10^{-1}$
a_1	$-4.90763093 \times 10^{-1}$	$-4.25676538 \times 10^{-1}$	$-3.54330127 \times 10^{-1}$	$-5.03060550 \times 10^{-1}$
a_2	$8.21319962 \times 10^{-2}$	$1.26614839 \times 10^{-1}$	$1.28857743 \times 10^{-1}$	$6.80197941 \times 10^{-2}$
a_3	$4.05187572 \times 10^{-2}$	$5.49262837 \times 10^{-3}$	$-2.32907961 \times 10^{-2}$	$7.06849424 \times 10^{-2}$
a_4	$-2.18593854 \times 10^{-2}$	$-2.38591622 \times 10^{-2}$	$-1.29482971 \times 10^{-2}$	$-3.22189277 \times 10^{-2}$
a_5	$-2.03733608 \times 10^{-3}$	$5.87763608 \times 10^{-3}$	$8.06838743 \times 10^{-3}$	$-6.13437273 \times 10^{-3}$
a_6	$3.83117056 \times 10^{-3}$	$1.04964297 \times 10^{-3}$	$-1.71191617 \times 10^{-3}$	$7.80976649 \times 10^{-3}$
a_7	$-1.13723230 \times 10^{-3}$	$-7.34668347 \times 10^{-4}$	$1.21773240 \times 10^{-4}$	$-2.32303732 \times 10^{-3}$
a_8	$1.48138379 \times 10^{-4}$	$1.27423841 \times 10^{-4}$	$6.98611684 \times 10^{-6}$	$3.09704825 \times 10^{-4}$
a_9	$-7.47896514 \times 10^{-6}$	$-7.64282498 \times 10^{-6}$	$-1.04438514 \times 10^{-6}$	$-1.60218268 \times 10^{-5}$

TABLE AIII. Polynomial coefficients for collision integral ratios in Eq. (A7) using the curve-fit expression in Eq. (A14).

	A^*	B^*	C^*
a_0	$9.79658841 \times 10^{-2}$	$1.75686064 \times 10^{-1}$	$-1.78376712 \times 10^{-1}$
a_1	$-1.18199219 \times 10^{-2}$	$-1.14468260 \times 10^{-1}$	$6.34778582 \times 10^{-2}$
a_2	$-1.48319945 \times 10^{-2}$	$1.91754719 \times 10^{-2}$	$4.50384957 \times 10^{-2}$
a_3	$2.99553485 \times 10^{-2}$	$3.49310192 \times 10^{-2}$	$-3.25043336 \times 10^{-2}$
a_4	$-9.78651731 \times 10^{-3}$	$-1.83923142 \times 10^{-2}$	$-3.84999163 \times 10^{-3}$
a_5	$-4.22994722 \times 10^{-3}$	$-9.39068490 \times 10^{-5}$	$7.47623838 \times 10^{-3}$
a_6	$3.85789124 \times 10^{-3}$	$2.60749721 \times 10^{-3}$	$-1.93716103 \times 10^{-3}$
a_7	$-1.11340927 \times 10^{-3}$	$-8.89422926 \times 10^{-4}$	$7.52217690 \times 10^{-5}$
a_8	$1.47279247 \times 10^{-4}$	$1.27670145 \times 10^{-4}$	$3.32052347 \times 10^{-5}$
a_9	$-7.56315066 \times 10^{-6}$	$-7.01803668 \times 10^{-6}$	$-3.48345912 \times 10^{-6}$

represented over the range $0.3 \leqslant \overline{T} \leqslant 100$ by a ninth-order polynomial expression of the form

$$\ln \Omega^{(i,j)} = a_0 + a_1\chi + a_2\chi^2 + a_3\chi^3 \cdots + a_9\chi^9,$$

(A14)

where $\chi = \ln \overline{T}$. The polynomial coefficients corresponding to this expression are listed in Table AII.

The collision integral ratios appearing in Eq. (A7) are not well predicted using the polynomial expressions

for the $\Omega^{(i,j)}$ computed via Eq. (A14). The quantities A^*, B^*, and C^* are used frequently enough in transport calculations that their values have also been tabulated as functions of the reduced temperature $\overline{T}$.[22] These tabulated values of the collision integral ratios have been fit to polynomial expressions of the form in Eq. (A14); that is, the natural logarithms of A^*, B^*, and C^* are fit to ninth-order polynomials in χ. The polynomial coefficients corresponding to these fits are listed in Table AIII.

2010

J. Mater. Res., Vol. 10, No. 8, Aug 1995